CTAB assisted synthesis of $MnFe_2O_4@ SiO_2$ nanoparticles for magnetic hyperthermia and MRI application

Roya Kavkhani [a], Abdollah Hajalilou [a,b,*], Ebrahim Abouzari-Lotf [c], Liliana P. Ferreira [d,b],
Maria Margarida Cruz [b], Mostafa Yusefi [e], Elahe Parvini [f], Alireza Bali Ogholbeyg [a],
Umi Nabilah Ismail [g]

[a] *Department of Materials Eng., University of Tabriz, Tabriz 51666-16471, Iran*
[b] *Biosystems and Integrative Sciences Institute (BioISI), Faculdade de Ciências,Universidade de Lisboa, Campo Grande, 1749-016 Lisboa, Portugal*
[c] *Karlsruhe Institut of Technologie (KIT), Institute of Nanotechnology (INT), Hermann-von-Helmholtz-Platz 1,76344 Eggenstein-Leopoldshafen, Germany*
[d] *Department of Physics, University of Coimbra, 3004-516 Coimbra, Portugal*
[e] *Malaysia-Japan International Institute of Technology, Universiti Teknologi Malaysia, Jalan Sultan Yahya Petra, 54100 Kuala Lumpur, Malaysia*
[f] *Department of Physical Chemistry, Faculty of Chemistry, University of Tabriz, Tabriz 51666-16471, Iran*
[g] *Department of Biomedical Imaging, Faculty of Medicine, University of Malaya, 50603 Kuala Lumpur, Malaysia*

ARTICLE INFO

ABSTRACT

Magnetic fluid hyperthermia (MFH) has been proven as a promising cancer therapeutic approach in conjunction with chemotherapy or physiotherapy in patients. The research to find innovative materials with a higher specific absorption rate (SAR) to reduce the dose of magnetic nanoparticles in tumor treatment through MFH while being also adequate for Magnetic Resonance Imaging (MRI) is important. Herein, $MnFe_2O_4$ NPs were synthesized with different sizes, using NaOH or NH_4OH as a reducing agent, via a green-assisted hydrothermal route. A tetraethyl orthosilicate with the assist of cetrimonium bromide was used to fabricate $SiO_2 @MnFe_2O_4$ NPs. Based on the Mössbauer and XRD results an undesired amount of α-Fe_2O_3 was found in the samples synthesized with NH_4OH. Concentration-dependent cellular toxicity values were evaluated by invitro 3-(4,5 dimethylthiazol-2-yl)−2,5-diphenyltetrazolium bromide (MTT) assay on A549 cells, where bare and silica coated nanoparticles exhibited non-toxicity below 691 µg/mL and 566 µg/mL, respectively. The ability of bare $MnFe_2O_4$ as the MRI contrast agent was higher compared to the silica-coated sample. The heating efficiency of the ferrofluids was recorded at 128 kHz and 10 kA/m and the highest SAR value was 39 W/g for the pristine $MnFe_2O_4$ NPs, making them promising potential materials in MRI and cancer treatment.
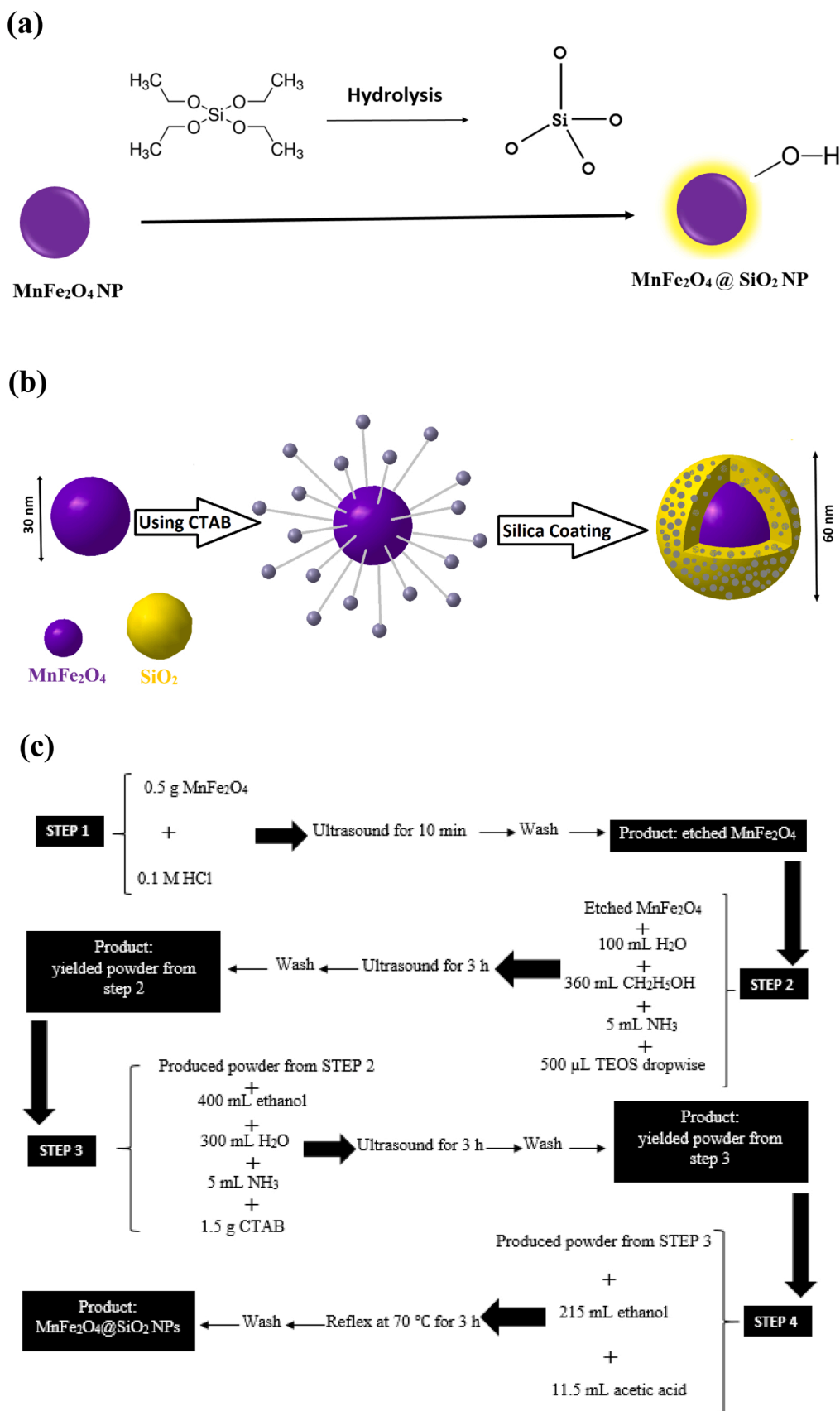
1. Introduction

There is always a demand to develop innovative materials and methods to mitigate tumors or cancer in human societies. Magnetic resonance imaging (MRI) is a non-invasive important technique for the diagnosis and post-therapy assessment of a variety of diseases [1]. The MRI technique offers several advantages such as excellent temporal and spatial resolution, the lack of exposure to radiation, rapid in vivo acquisition of images, and a long effective imaging window. However, MRI is much less sensitive than nuclear medicine or fluorescence imaging to monitor small tissue lesions, molecular activity, or cellular activities [2]. The use of superparamagnetic nanoparticles in contrast agents for MRI improved the quality of their results and the combination of mesoporous silica with magnetic nanoparticles and other functional molecules culminated in new types of hybrid nanocarrier platforms for cell imaging, diagnosis, and therapy [2]. Furthermore, the heat generation of magnetic nanoparticles (MNPs) under an alternate magnetic field is considered a promising therapy for tumor or cancer treatment, in conjunction with chemotherapy and radiotherapy [3]. In this technique, magnetic fluid hyperthermia (MFH), the MNPs are dispersed in a nontoxic carrier fluid and subjected to an alternating magnetic field (AMF). The heat generation is typically quantified by the specific absorption rate (SAR) or specific loss power (SLP), which is defined as the thermal power per unit mass of magnetic materials [4–6]. Its magnitude depends on both the intrinsic properties of the MNPs, such as phase composition, shape, magnetic anisotropy, mean size, and size

---

* Corresponding author at: Department of Materials Eng., University of Tabriz, Tabriz 51666-16471, Iran.
E-mail address: e.hajalilou@yahoo.com (A. Hajalilou).

(a)

H₃C, CH₃ — Hydrolysis

MnFe₂O₄ NP

MnFe₂O₄ @ SiO₂ NP

(b)

30 nm

Using CTAB

Silica Coating

60 nm

MnFe₂O₄   **SiO₂**

(c)

STEP 1

0.5 g MnFe₂O₄
+
0.1 M HCl

Ultrasound for 10 min → Wash → Product: etched MnFe₂O₄

STEP 2

Etched MnFe₂O₄
+
100 mL H₂O
+
360 mL CH₂H₅OH
+
5 mL NH₃
+
500 µL TEOS dropwise

Product: yielded powder from step 2 ← Wash ← Ultrasound for 3 h

STEP 3

Produced powder from STEP 2
+
400 mL ethanol
+
300 mL H₂O
+
5 mL NH₃
+
1.5 g CTAB

Ultrasound for 3 h → Wash → Product: yielded powder from step 3

STEP 4

Produced powder from STEP 3
+
215 mL ethanol
+
11.5 mL acetic acid

Product: MnFe₂O₄@SiO₂ NPs ← Wash ← Reflex at 70 °C for 3 h

Fig. 1. (a) Schematic of the synthetic procedure for MnFe₂O₄@mSiO₂ core-shell, (b) the function of CTAB in forming SiO₂ coating on MnFe₂O₄ NPs, and (c) flowchart of the experimental procedure used for making MnFe₂O₄@mSiO₂ NPs.

distribution, and also on the extrinsic characteristics of the process, such as alternating magnetic field parameters, like amplitude and frequency [7,8]. To kill the cancerous cells, their temperature should rise to 42–48 °C for 30–60 min [9], the cancerous cells are more sensitive to high temperatures than the healthy cells [7].

For MFH, research focuses on magnetite and maghemite NPs, which have been proved to be well tolerated by the human body [10]. On the other hand, the magnetic properties of the iron oxide NPs are difficult to control by the synthesis process. A better alternative is the use of complex magnetic oxides with physico-chemical and magnetic properties controlled by compositional variations [11]. In this regard, ferrites with a general formula MFe_2O_4, where M stands for the divalent or trivalent cations of transition metals, such as Fe, Ni, Mn, etc., with spinel structure with 64 tetrahedral and 32 octahedral positions available for cations in one unit cell, have been considered [12–14]. The cation types and their distribution at tetrahedral and octahedral sites play an overwhelming role in the physical and chemical properties of spinel ferrite NPs. Based on the cation type and distribution, at both the foregoing-mentioned sites, three types of spinel structures (normal, inverse, and mixed) can be obtained [15]: normal spinel, where the structure consists of eight tetrahedral voids occupied by one M^{2+} and four octahedral voids occupied by two Fe^{3+} cations, while the oxygen anions are arranged in a cubic close-packed structure. In the inverse spinel, half of Fe^{3+} and all M^{2+} are distributed at octahedral sites and the remaining half of Fe^{3+} occupy the tetrahedral sites. In terms of mixed ferrites, mixtures of both oxidation states exist at both sites, depending on the synthesis method [16,17]. Manganese ferrite ($MnFe_2O_4$) is an example of a mixed ferrite with 80% normal and 20% inverse structure which acts as an inverse spinel [18] and the preparation method of manganese ferrite MNPs determines their final shape, size distribution, surface chemistry, and magnetic properties [19–21]. There are an extensive diversity of synthesis methods, ranging from electrospinning [22], sol-gel [23,24], coprecipitation [25–27], solid-state reaction, such as high-energy ball milling [28], to hydrothermal reaction [29,30], the majority of the magnetic NPs being synthesized at nanometric scale because of the large surface-to-volume ratio which yields favorable properties for biomedical applications [23]. The hydrothermal technique is a promising approach to achieve this target.

In addition, it is worth pointing out that ferrite NPs are generally toxic, thus surface modification is required to use them in the human body [31]. A variety of biocompatible materials have been developed for hyperthermia application, e.g., inorganic compounds such as SiO_2 [32]. Amongst the wide spectrum of surface modification agents, the mesoporous silica holds a unique position on account of its well-defined pore structures, stability, nontoxicity, hydrophilicity, biocompatibility, chemical inertness, low cost, and facile functionalization [33]. Thus, the synthesis of magnetic $MnFe_2O_4$ cores by tailoring the silica shell is of particular interest in magnetic fluid hyperthermia due to $MnFe_2O_4$ superior magnetization [34] and biocompatibility of SiO_2 [33].

The main draw of this study is to synthesize $MnFe_2O_4$ NPs via the hydrothermal method (using NH_4OH and $NaOH$ as reducing agents) and coat them with SiO_2. This is followed by the investigation of the effect of the coating process on structure, morphology, toxicity, magnetic properties, hyperthermia efficiency, and MRI properties of the fabricated materials.

2. Experimental

2.1. Materials

The chemical reagents used in this work were iron (III) chloride hexahydrate ($FeCl_3 \cdot 6H_2O$, Sigma-Aldrich, CAS-No: 10025–77–1), Manganese (II) nitrate tetrahydrate ($Mn(NO_3)_2 \cdot 4H_2O$, Sigma-Aldrich, CAS-No: 20694–39–7.), sodium hydroxide (NaOH, Sigma-Aldrich, CAS-No: 1310–58–3), ammonium hydroxide (NH_4OH, Sigma-Aldrich, CAS-No: 1336–21–6) and deionized water.

2.2. Synthesis of magnetic nanoparticles (MNPs)

2.2.1. Synthesis of $MnFe_2O_4$ NPs

$MnFe_2O_4$ NPs were synthesized under different hydrothermal conditions using NaOH or NH_4OH as precipitating agents, the corresponding samples being named MF_1 and MF_2, respectively. $FeCl_3.6 H_2O$ and $Mn(NO_3)_2.4 H_2O$, with stoichiometric ratio 2:1, were dissolved in 80 mL of deionized water with the assistance of magnetic stirring at room temperature. The pH value of the obtained solution was adjusted to 11 by adding dropwise 5 M NaOH or NH_4OH. The obtained homogeneous mixture was then transferred into a 100 mL-sealed Teflon-lined stainless autoclave and heated at 190 °C for 24 h. After cooling to room temperature, the obtained precipitate was washed several times with distilled water and finally dried at 60 °C for 15 h.

2.2.2. Synthesis of $MnFe_2O_4$ @mSiO_2 nanoparticles

$MnFe_2O_4$ @mSiO$_2$ (MFS$_1$ and MFS$_2$) NPs were prepared by hydrolysis of Tetraethyl orthosilicate (TEOS) on the surface of both MF_1 and MF_2, respectively [32]. In brief, 0.5 g of the $MnFe_2O_4$ powder was dispersed in 0.1 M HCl aqueous solution, and the mixture was ultrasonically treated for 10 min (Step1). To form the initial SiO$_2$ layer on the $MnFe_2O_4$, for 3 h (Fig. 1a), the $MnFe_2O_4$ NPs were then washed with deionized water and dispersed in a solution of 100 mL deionized water, 360 mL ethanol, 5 mL ammonia solution, and 500 μL TEOS using an ultrasonic bath for 3 h (Fig. 1a). After the magnetic nanoparticles were washed with deionized water (Step 2) and the obtained powders were dispersed into the mixed solution of 400 mL ethanol, 300 mL H$_2$O, 5 mL ammonia solution, 1.5 g cetrimonium bromide (CTAB), which is a strong cationic surfactant for dispersing, and pore-making agent to provide ordered mesoporous silica shell [35–37]. After 2000 μL TEOS was dropped into the reaction solution. The mixture was then submitted to an ultrasonic bath for 3 h. Fig. 1b illustrates the role of CTAB in forming a porous SiO$_2$ layer on $MnFe_2O_4$ NPs. The obtained magnetic nanoparticles were collected with a magnet and washed several times with deionized water (Step 3). To remove the CTAB, the $MnFe_2O_4$ @mSiO$_2$ NPs were mixed with ethanol and acetic acid (95:5) and heated at 70 °C for 3 h in 3-necked reflux. Finally, the last purifications were performed by washing produced $MnFe_2O_4$ @mSiO$_2$ with deionized water, ethanol, and methanol several times, followed by drying at 60 °C for 24 h (Step 4). These processes are schematically shown in Fig. 1c. The silica formation mechanism on $MnFe_2O_4$ NPs proceeds by nucleation and growth [38]. Nucleation is the process in which the first insoluble species, probably doubly hydrolyzed TEOS monomers, are formed and precipitated. Growth, on the other hand, occurs both by the addition of newly hydrolyzed monomers to these nuclei and by the aggregation of small particles to form larger ones (not to be confused with $MnFe_2O_4$ NP aggregation). Although these two processes are closely related and cannot be separated entirely, their relative contribution to the whole reaction can be modified to some extent by manipulating the reaction conditions.

2.3. Characterization

The Fourier-transform infrared spectroscopy (FTIR) measurements were carried out on a BUCKER TENSOR 27 instrument to identify the surface nature of MNPs in the range of 400–4000 cm^{-1}.

A SIEMENS, D5000X-Ray diffractometer (XRD) with Cu-Kα radiation ($\lambda = 1.54059$ Å) was used to study the phase formation and the structural changes. To estimate the crystallite size (D) of the samples, from the peak width, the Scherrer relation was considered [39]:

$$D = \frac{0.9\lambda}{b\cos\theta} \qquad (1)$$

where b is the full width of each peak at half maximum (FWHM), λ is the wavelength and θ is the corresponding Bragg angle [39]. The lattice
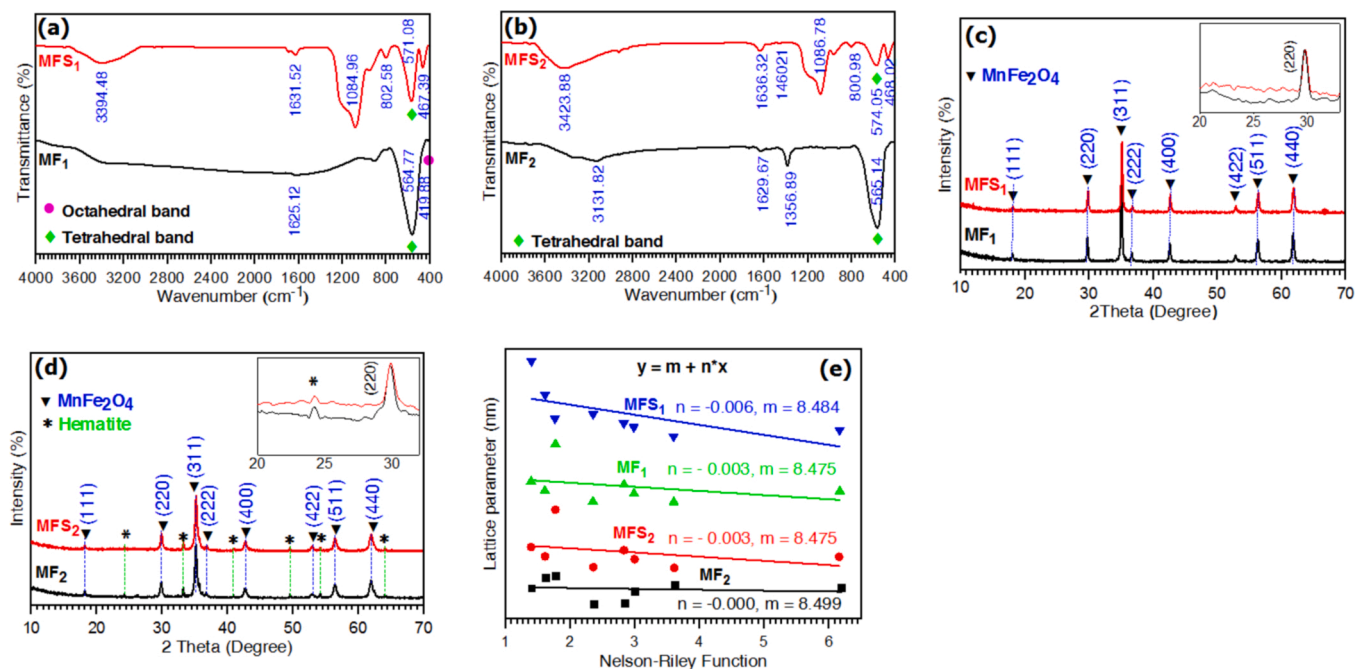
Fig. 2. FTIR spectra of the samples synthesized with NaOH (a) MF1 and MFS1 and with NH4OH (b) MF2 and MFS2, (c and d) XRD patterns of the same samples with inset showing the corresponding amplitude in log scale between 20 and 30 degrees, (e) Lattice parameter versus Nelson-Riley equation.

parameter (a) of the as-synthesized samples, was obtained considering Bragg's law (2 and 3) and Nelson-Riley (3) equations [15,40,41]:

$$n\lambda = 2d\sin\theta \tag{2}$$

$$F(\theta) = \frac{1}{2} \cos^2\theta(\csc\ \theta\ +\ 1\Big/\theta) \tag{3}$$

The chemical composition of the core-shell and bare particles was accessed by energy dispersive X-ray analysis (EDX)/mapping from BRUKER XFlash® 6 | 10. Field-emission scanning electron microscopy (FESEM) analyses were carried out to study the morphology of the samples using the FEI Nova NanoSEM 450. The nanoparticles were also characterized by transmission electron microscopy (TEM) using a Hitachi H8100 with a digital image acquisition microscope. The particle size distributions of the samples were determined statistically from the size measurements of around 100 nanoparticles using the Image J software.

The Brunauer–Emmett–Teller (BET) analysis was accomplished through a physisorption analyzer (ASAP 2020, Micromeritics, USA). The samples were first degassed at 35 °C under vacuum for 24 h and then, the nitrogen adsorption-desorption isotherms of the degassed sample were evaluated at 77 K. The BET calculation was conducted as a relative pressure range from 0.06 to 0.20. The Barrett–Joyner–Halenda (BJH) method, with the volume absorbed under a relative pressure (P/Po = 0.98), was employed to measure pore size distribution as total pore capacity.

Magnetic characterization of the samples was performed using a QD-MPMS SQUID magnetometer. The magnetization as a function of temperature (M-T curves) was recorded in the temperature range of 10–380 K by applying a small magnetic field of 5 mT, after zero magnetic field (ZFC) cooling and after field cooling (FC). Hysteresis curves were obtained at 300 K for magnetic fields up to 5.5 T.

The ^{57}Fe Mössbauer spectra were collected at room temperature in transmission mode using a conventional constant acceleration spectrometer and a 50 mCi 57Co source in a Rh matrix. The velocity scale was calibrated using an α-Fe foil and the spectra were fitted using the WinNormos Program.

To investigate the specific absorption rate (SAR), homogeneous MNPs suspensions in distilled water were prepared for three different concentrations (4, 6, and 8 mg/mL) and the time-dependent temperature curves were recorded using a home-made set up for alternate magnetic fields with 128 kHz frequency and 10 kA/m amplitude.

For MRI analysis, Five different concentrations of 10, 20, 30, 40 and 50 µg/mL were prepared in 10 mL of 1% agarose solution for each sample. The samples were dispersed in a phantom that was scanned using a clinical 3 T MRI (MAGNETOM Prisma, Siemens Healthcare, Germany) using a turbo-spin-echo sequence (TSE) with a repetition time (TR) = 3000 ms, 14 echo time (TE) starting from 10 to 140 ms with increment of 10 ms and 2 mm slice thickness.

A custom-written MATLAB program was used to analyze the obtained MRI images. Signal intensities of each phantom were curve-fitted with time to obtain transverse relaxation times, T_2. Relaxation rates, R_2 inverse of T_2 for each sample concentration were then used to measure r_2 values according to the following equation:

$$R_{2_i} = r_2 C_i + R_{2_0} \tag{4}$$

where R_{2i} is the transverse relaxation rate (s^{-1}) for the tube with concentration, C_i (µg/mL). R_{2o} is the expected relaxation rate when no sample was dispersed in the phantom.

2.4. Cell experiments

2.4.1. Cell culture

The cells were cultured in RPMI medium containing 10% bovine serum and 1% antibiotic solution of Penicillin Strodemicin and stored in an incubator at 37 °C under 5% CO₂ condition.

2.4.2. Cytotoxicity study

The MTT assessment using 3- (4,5-dimethylthiazol-2-yl) 2,5-diphenyltetrazolium bromide was employed to evaluate the cytotoxicity of MF_1 and MFS_1 NPs. The viability of A549 cells was investigated. In this method, 10,000 cells were transferred to 96-well plates and incubated for 24 and 48 h prior to adding the nanoparticles. The synthesized NPs were processed and applied in various concentrations (0, 25, 50, 75, 50, 100, 125, 150, 175 µg/mL), and the treated cells were incubated for 24 and 48 h. After that, 20 µL of MTT solution (at a concentration of

5 mg/mL) was added to each well of the plate and was incubated for 4 h, followed by the addition of 200 μL of dimethyl sulfoxide. After 15 min of incubation, the optical absorption of each well was measured at the wavelength of 570 nm and a filter of 630 nm in the ELAIZE reader system. According to the following equation, the results were calculated as the percentage of cell survival [42]:

$$cell\ survival = (\frac{light\ adsorption\ of\ the\ treatment\ group}{light\ adsorption\ of\ the\ control\ group}) \times 100 \qquad (5)$$

The experiments were repeated three times and the data were reported as mean $\pm$ deviation from the standard. Graphs were plotted using GraphPad Prism2018 software.

2.5. DAPI-stained

After the course of incubation, the cells were treated with $MnFe_2O_4$ and $MnFe_2O_4$ @mSiO_2 NPs solutions, slowly washed with PBS and then 1% formalin was added for fixing the cells and after they were kept for 20 min in the refrigerator. Then, the obtained pellet was exposed to air at room temperature for 5 min. Formalin was gently taken out from the corners of the 24-well plate and then 4% of Triton was added to it (Triton increases permeation of the DAPI cell membrane). After 15 min, the cells were removed from Triton and washed with PBS. Finally, 1% DAPI was added and after 20 s it was rewashed with PBS. Due to the light sensitivity of the DAPI, this step was performed in a dark environment. Cell nucleus morphology and changes in treatment were examined by Inverted Fluorescent Microscopes.

All the steps were repeated at least three times. INSTATE 3 software was used to analyze the data using ANOVA ONE-WAY. A p-value of less than 0.05 was considered statistically significant.

3. Results and discussion

3.1. Absorption band evaluation by FT-IR spectroscopy

To evaluate the chemical absorption bands of the as-synthesized samples, the FTIR spectra were recorded in the range of 400–4000 cm^{-1} (Fig. 2a and b). Two main absorption bands associated with atomic vibration of metal and oxygen ions occur at around 600 cm^{-1} for the tetrahedral metal positions, and 400 cm^{-1} for the octahedral ones [32,39,43]. In the case of the $MnFe_2O_4$ NPs synthesized with NaOH (Fig. 2a), the two absorption bands were observed around 419 and 564 cm^{-1}, respectively, indicating that the Fe ions are distributed between octahedral and tetrahedral sites [39] indicating the $MnFe_2O_4$ phase formation, and in agreement with XRD results. The FTIR spectrum also shows a characteristic peak at 1625 cm^{-1}, which is associated with the O–H stretching bond [32,44]. Fig. 2b shows the spectra of synthesized $MnFe_2O_4$ NPs with NH_4OH. According to Fig. 2a and b, it is evident that different absorption bands appear, the position being shifted due to influence of the reduction agent. Contrary to the as-synthesized $MnFe_2O_4$ with NaOH, the Mn-ferrite prepared with NH_4OH, displays no peak around 400 cm^{-1}. The absorption peak related to the vibrations of tetrahedrally coordinated metal ions in the spinel structure appears at 565 cm^{-1} [42]. The band at 1629 cm^{-1} is associated with the previous 1625 cm^{-1} and a new absorption peak appears at 3131 cm^{-1}, confirming the presence of O-H groups [32,39]. Another extra peak at 1386 cm^{-1} is associated with the symmetric vibrations of the NO_3 [42].

In the case of $MnFe_2O_4$ @mSiO_2 samples (MFS_1 and MFS_2), some extra peaks emerge compared with uncoated samples. As seen in Fig. 2a and b, the peak positions of MFS_2 appear at wave number values slightly higher than in MFS_1. The absorption bands at 802 and 800 cm^{-1} identify the vibration modes of Si-OH of MFS_1 and MFS_2, respectively. The peaks observed at 1084 and 467 cm^{-1} are attributed to Si-O-Si or Si-O of MFS_1 and appear in MFS_2 at 1086 and 468 cm^{-1} [8,31]. It is worth mentioning that the supplementary peak at 1460 cm^{-1} in MFS_2 sample is due to

Table 1
FTIR absorption bands of $MnFe_2O_4$ and $MnFe_2O_4$ @mSiO_2 samples and their assignment.

Assignment	Band position (cm^{-1})				Reference
	MF_1	MF_2	MFS_1	MFS_2	
Octahedral band	419	–	–	–	[32,39, 43]
Tetrahedral band	564	565	571	574	[39,42]
Vibration of Si-OH	–	–	802	800	[8,31]
Vibration of Si-O-Si and Si-O	–	–	1084 & 467	1086 & 468	[8,31]
Symmetric vibration of NO_3	–	1386	–	–	[42]
Vibrations of CH_3–N^+	–	–	–	1460	[45]
Vibration of O–H	1625	3131 & 1629	3390 & 1631	3423 & 1636	[32,44]

asymmetric C–H scissoring vibrations of a CH_3–N^+ moiety in CTAB [45]. The new peaks indicate the complete formation of a silica shell onto the surface of $MnFe_2O_4$ [35,46]. Described results are summarized in Table 1.

3.2. X-Ray diffraction analysis

The X-ray diffraction patterns of the synthesized $MnFe_2O_4$ under different hydrothermal conditions (MF_1 and MF_2) and of the corresponding silica-coated samples (MFS_1 and MFS_2) are illustrated in Fig. 2c and d. All diffraction peaks of MF_1 NPs (Fig. 2c) fit perfectly with the standard spinel $MnFe_2O_4$ (JCPDS Card no. 01–074–2403). Whereas, in the case of the synthesized MF_2 NPs (Fig. 2d), a few extra peaks show the presence of a second phase identified as hematite. In silica-coated samples (MFS_1, MFS_2), a significant amorphous component is detected in the XRD patterns, with a broad peak between 20 and 30° depicting the presence of silica [47].

To determine the lattice parameters with precision, the lattice parameter determined from applying Bragg relation to each reflection was plotted versus the Nelson-Riley function (Fig. 2e). The lattice parameter was determined from the extrapolation to zero and, with other properties of the synthesized and silica-coated samples (MF_1, MF_2, MFS_1, MFS_2) are presented in Table 2. For all samples, the calculated lattice parameters are similar and in agreement with the lattice parameters of 8.454 Å, 8.479 Å, and 8.49 Å reported for $MnFe_2O_4$ synthesized via double ceramic processing technique [48] and chemical co-precipitation route [49].

The calculated crystallite size using the Scherrer formula of synthesized $MnFe_2O_4$ NPs with NaOH (MF_1) is 28 nm whereas the diameter of synthesized $MnFe_2O_4$ NPs with NH_4OH (MF_2) is 18 nm. The reported crystallite size of $MnFe_2O_4$ NPs synthesized with other methods is widely different. For example, in the case of the sol-gel auto-combustion route [50] the obtained crystallite size is reported about 24.5 nm, whereas 12 nm is the crystallite size of $MnFe_2O_4$ NPs synthesized by the polymer-pyrolysis method [51]. The crystallite size for coated samples is equal to the corresponding uncoated $MnFe_2O_4$ NPs (see Table 2). For silica coating onto the NPs, an increase [32] and also a decrease [52] in the crystallite size of samples are reported.
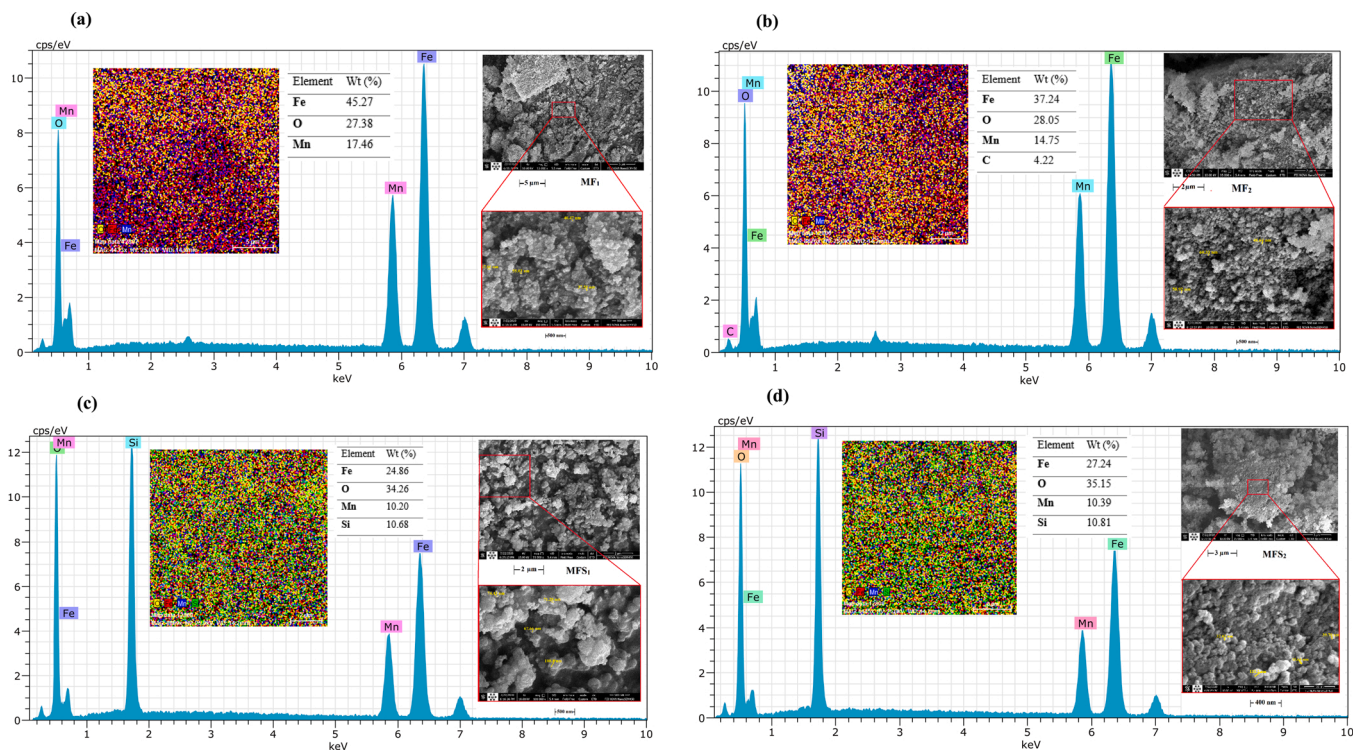
3.3. Morphological and compositional observation

3.3.1. FESEM/ EDX/ mapping and TEM

The FESEM micrographs (with different magnifications) and EDX spectra and mapping of synthesized and coated $MnFe_2O_4$ NPs samples are illustrated in Fig. 3. As is shown in Fig. 3a and b, the particles of MF_1 and MF_2 have irregular shapes. EDX analysis confirmed the expected (Fe, Mn, O) composition. The FESEM images of silica-coated $MnFe_2O_4$, MFS_1, and MFS_2, (Fig. 3c and d) show irregular particle morphology.

Table 2

A summary of the magnetization and physical details of $MnFe_2O_4$ and $MnFe_2O_4$ @$mSiO_2$ nanoparticles in different references.

M_S (Am²/kg)		$\mu 0H_C$ (mT)		T_B (K)		Crystalline size (nm)		Lattice parameter (Å)		Reference
$MnFe_2O_4$	$MnFe_2O_4$ @$mSiO_2$	$MnFe_2O_4$	$MnFe_2O_4$ @$mSiO_2$	$MnFe_2O_4$	$MnFe_2O_4$ @$mSiO_2$	$MnFe_2O_4$	$MnFe_2O_4$ @$mSiO_2$	$MnFe_2O_4$	$MnFe_2O_4$ @$mSiO_2$	
70	44	6	6	330	360	28	28	8.499	8.475	This study (synthesized via NaOH)
64	40	4	6	330	360	18	17	8.475	8.484	This study (synthesized via NH₄OH)
50	20	~0	~0	–	–	–	9.8	–	–	[53]
54	44	~0	~0	–	–	35	60	–	–	[32]
37	20	~0	~0	–	–	–	–	–	–	[46]

Fig. 3. SEM-EDX spectrum and mapping of (a) synthesized $MnFe_2O_4$ via NaOH (MF_1), (b) synthesized $MnFe_2O_4$ via NH_4OH (MF_2), (c) silica-coated of MF_1 (MFS_1), and (d) silica-coated of MF_2 (MFS_2).

Contrary to bare manganese ferrite nanoparticles the silica-coated nanoparticles are not aggregated as flakes, indicating the role of the coating layer that prevents the MNPs from agglomeration. EDX/mapping analysis of MFS_1 and MFS_2 samples revealed the presence of Si in addition to Fe, Mn, and O elements. The TEM images of the samples are presented in Fig. 4a. The average particle sizes determined for MF_1 and MF_2 NPs are 27 and 31 nm, respectively. On the other hand, in the case of MFS_1 the obtained histogram shows a bimodal distribution of the particle sizes, with maxima at 50 nm and around 150 nm. For the MFS_2 the obtained average diameter is 70 nm with a maximum at around 50 nm. TEM micrographs confirmed the complete formation of silica shells on $MnFe_2O_4$ NPs.

3.3.2. Mössbauer spectroscopy

The ^{57}Fe Mössbauer spectra of all four samples, acquired at room temperature and under zero applied magnetic field are presented in Fig. 4b, the results of the fitting procedures being shown in Table 3.

Significant features about the Mössbauer results are the confirmation, as also detected by XRD, of the presence of around 10% of hematite only in the samples prepared via NH_4OH (orange subspectrum in MF2 and MFS2). Apart from that, all spectra need two sextets of distributed

magnetic hyperfine fields (B_{hf}) to be properly fitted, one with isomer shift, δ, values close to 0.3 mm.s⁻¹ and a second one with δ values between 0.45 and 0.5 mm.s⁻¹. These features indicate, on one hand, the presence of iron ions both in tetrahedral and octahedral positions of the spinel structure and, on the other hand, the presence of iron ions of both valences, 3 + and 2 + . This, together will the high mean values of B_{hf} with not very broad distributions ([σ] between 5 and 9 T), is consistent with the fact that the NPs sizes are not very small, because below 10 nm, iron ions are normally all oxidized to 3 + .

3.3.3. BET

Fig. 5 demonstrates the BET results in the nitrogen adsorption/desorption isotherms and at synthesized Mn ferrite via NaOH (MF_1) and silica-coated (MFS_1) NPs and pore size distribution MFS_1. From Fig. 5a, the type (II) adsorption-desorption isotherm pattern of MF_1 indicates $MnFe_2O_4$ NPs are non-porous or macroporous [54], whereas, in Fig. 5b after coating with the silica shell, the isotherm alters to mesoporous type (IV) [55]. Supplementary, the pore size distribution curve of MFS_1 nanoparticle was sized between 2 and 50 nm, which is extra proof that the nanoparticle is mesoporous [56]. Although the high X-ray density and also the larger particle size of MFS_1 with comparison to MF_1, the

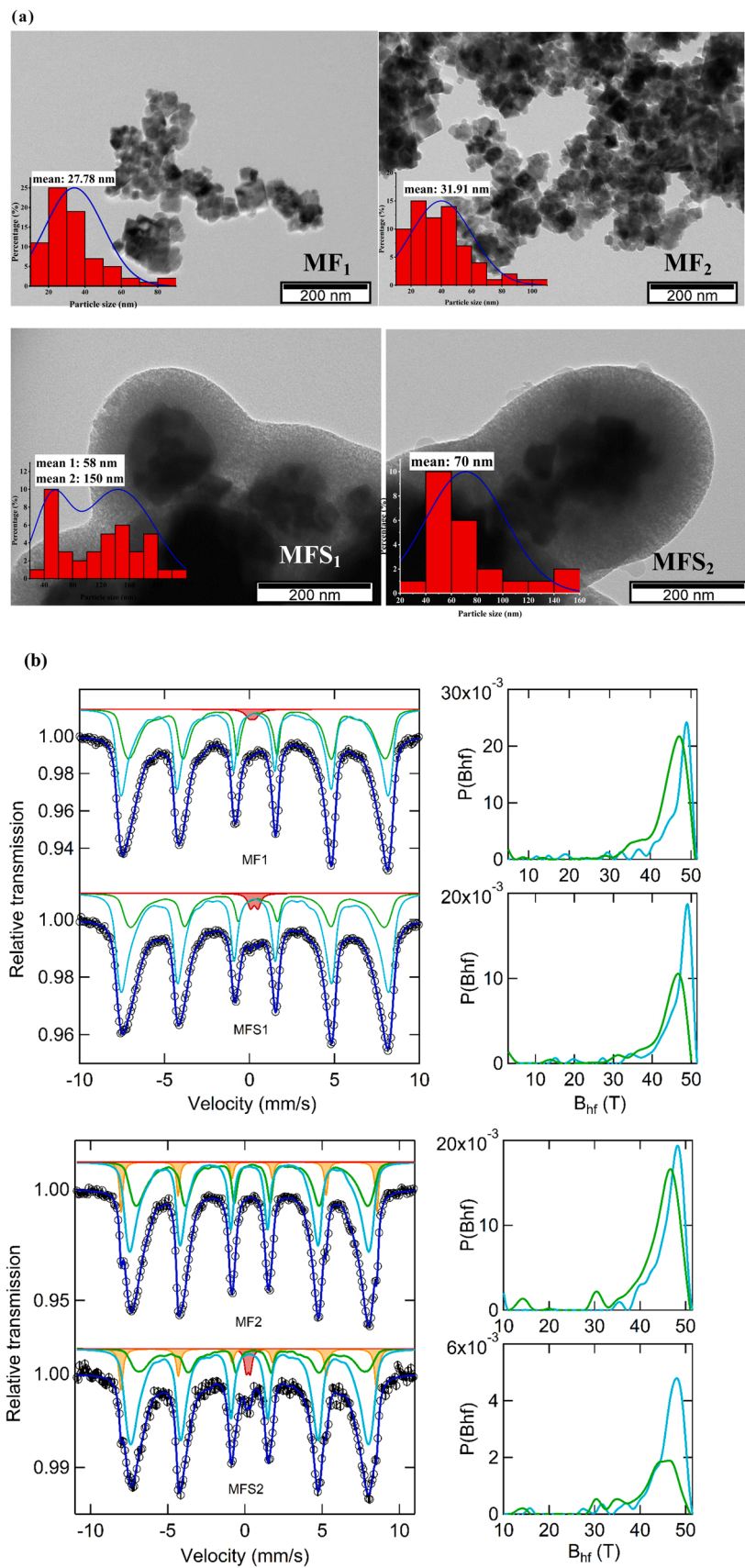**Fig. 4.** (a) TEM images of the as-synthesized MnFe$_2$O$_4$ NPs and coated ones, (b) ^{57}Fe Mössbauer spectra of all samples, collected at room temperature under zero applied magnetic field.

Table 3

Mössbauer hyperfine fitting parameters for all samples. $\langle B_{hf} \rangle$ [σ]: average magnetic hyperfine field and standard deviation of the magnetic field distribution; B_{hf}: hyperfine magnetic field; δ: isomer shift; ε: quadrupole shift; QS: quadrupole splitting; Γ: line width; I: relative area.

Sample	Site	$\langle B_{hf} \rangle$ [σ] /T	B_{hf} /T	δ /mm.s^{-1}	ε /mm.s^{-1}	QS /mm.s^{-1}	Γ /mm.s^{-1}	I /%
MF$_1$	blue	45 [7]	–	0.28(1)	0.01(1)	–	0.34	58.8
	green	44 [7]	–	0.45(1)	-0.02(1)	–	0.30	39.8
	red	–	–	0.16(3)	–	0.34(5)	0.4(1)	1.4
MFS$_1$	blue	46 [6]		0.31(1)	0.01(1)	–	0.39	69.4
	green	42 [9]		0.48(1)	-0.02(1)	–	0.37	28.6
	red	–		0.29(2)	–	0.43(3)	0.39(6)	2.0
MF$_2$	bleu	46 [5]	–	0.28(1)	0.01(1)	–	0.34	56.9
	green	43 [7]	–	0.47(1)	-0.01(2)	–	0.30	33.6
	orange	–	51.4(1)	0.37(1)	-0.20(1)	–	0.26(1)	9.5
MFS$_2$	bleu	45 [5]	–	0.29(1)	0.01(1)	–	0.38	67.0
	green	42 [7]	–	0.51(3)	-0.09(5)	–	0.30	21.2
	red	–	–	0.22(2)	–	0.26(4)	0.39(6)	9.5
	orange	–	51.3(1)	0.36(1)	-0.23(2)	–	0.29(7)	2.3
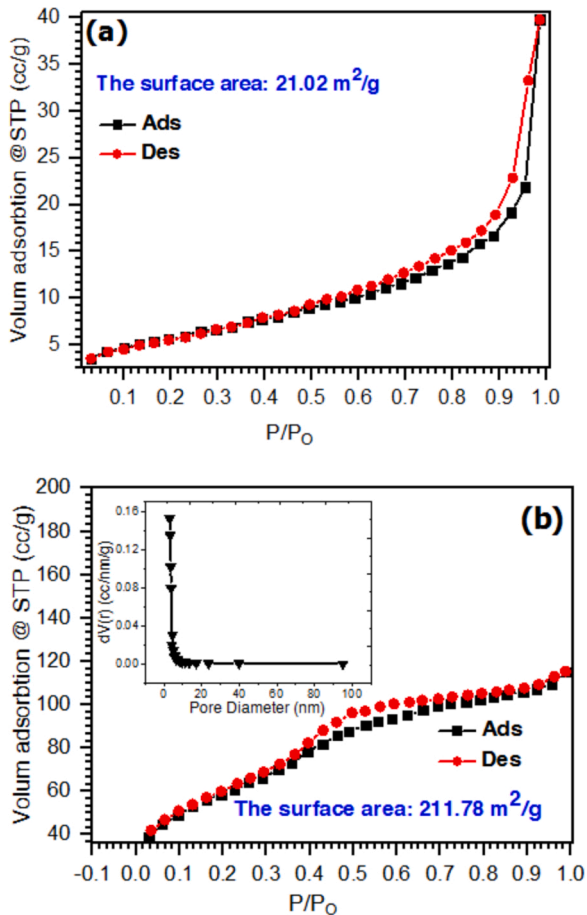
Fig. 5. Volume adsorption of (a) MF$_1$ and (b) MFS$_1$ versus relative pressure and pore size distribution.

BET surface area of bare MnFe$_2$O$_4$ NPs is 21.02 m^2/g and the surface area of silica-coated MnFe$_2$O$_4$ NPs is approximately 10 times greater than the uncoated NPs. The reason for this could be related to the role of CTAB in the coating which is caused the formation of mesoporous silica shells onto Mn-ferrite NPs (MnFe$_2$O$_4$ @mSiO$_2$).

3.4. Magnetic measurements

Fig. 6a shows the temperature dependence of ZFC-FC magnetization curves for synthesized MnFe$_2$O$_4$ NPs using NaOH (MF$_1$) and NH$_4$OH (MF$_2$) and for the silica-coated powders MFS$_1$ and MFS$_2$. All the samples show similar temperature dependence in the range of 10–380 K. The magnetization versus temperature increases in all the samples due to the progressive alignment of the NP magnetic moment in the applied field.

The main difference relies on the slope of the ZFC curves in the range 300–380 K, being much smaller in MF$_1$ than in MF$_2$. The ZFC curves of MFS$_1$ and MFS$_2$, exhibit the same behaviour of the corresponding bare NPs, MF$_1$ and MF$_2$, respectively. The lower magnetic moment of the silica-coated samples is due to the increase of mass associated with the presence of nonmagnetic silica [57].

Curves FC and ZFC join at the highest temperature and no maximum is observed at lower temperatures. The temperature corresponding to a peak maximum for a collection of monodisperse MNPs value of magnetization is known as the blocking temperature (T_B) [58]. Different T_B is expected since the samples are prepared in different conditions [59]. The results indicate that T_{max} will be reached above 380 K. The mean blocking temperature (T_B) for a collection of NPs assembly is reported to be less than the T_{max} and is given by $T_{max} = \beta T_B$, where β is a constant and depends on the distribution of blocking temperatures and on the strength of interparticle interactions [59,60]. Recently, the best methods of estimating T_B of particles is the point at which the rate of change of the difference ($\Delta M = M^{FC} - M^{ZFC}$) as a function of temperature is maximum, which occurs to the left of the peak [61]. Fig. 6b shows ΔM plots for the samples versus temperature indicating a smaller slope for the MF$_1$ and MFS$_1$ samples compared with MF$_2$ and MFS$_2$ which indicates wider T_B distribution for the former in comparison with the latter. The average T_B can be determined by the maximum of the symmetric of the first derivative of ΔM as a function of temperature [59,60]. According to Fig. 6c, the T_B is 330 K for the MF$_2$ and of the same order of magnitude but not so well defined for MF$_1$, whereas it is of the order of 360. K in MFS$_1$ and MFS$_2$. The shift in T_B can be related to a broader size distribution or an increase of the effective anisotropy constant (K_1) due to different strain and surface spin disorders, making them uniquely suitable for high-density data storage and hyperthermia applications [62,63]. A straight line in Fig. 6c describes non-interacting magnetic nanoparticles with uniaxial anisotropy [60].

The magnetic hysteresis loops of synthesized MnFe$_2$O$_4$ and silica-coated NPs are shown in Fig. 6d. The MF$_1$ has the highest spontaneous magnetization of all samples, about 70 emu/g. According to XRD results, this is explained by being the sample with larger particles. In the case of coated samples (MFS$_1$ and MFS$_2$), the smaller magnetization is due to the presence of Si-O diamagnetic layer on the surface of MnFe$_2$O$_4$ NPs. The thickness of the dead layer in iron oxide NPs was calculated, assuming spherical NPs, and using the spontaneous magnetization of the bulk material for the ordered region, M_{so}, and the spontaneous magnetization of the NPs, Ms. [39]:

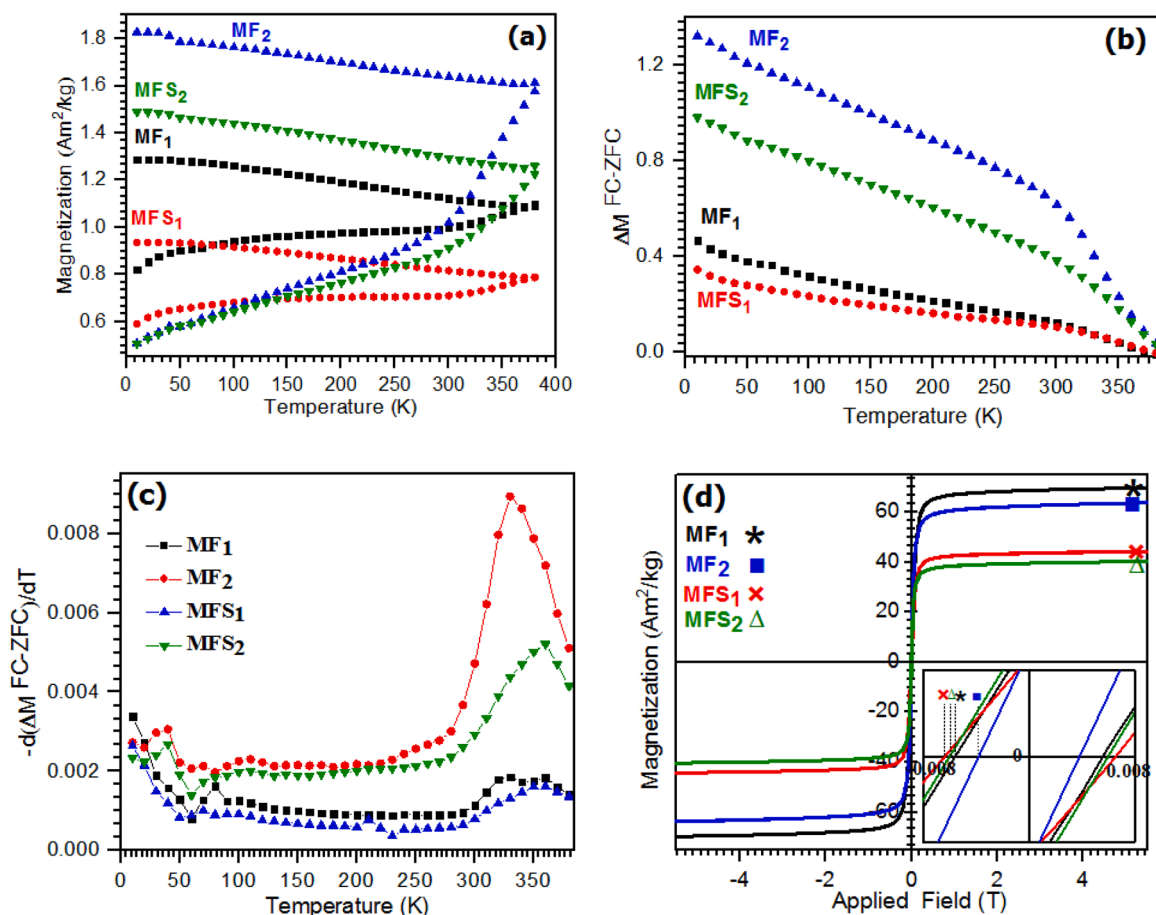$$t = \frac{d}{2}\left[1 - \left(\frac{M_s}{M_{so}}\right)^{\frac{1}{3}}\right] \tag{6}$$

Fig. 6. (a) FC and ZFC magnetization curves, (b) ΔM plots versus temperature, (c) d(ΔM)/dT plots versus temperature, and (d) a room temperature M-H hysteresis of the samples.

where, d is the particle diameter calculated from the Scherrer equation. The thickness of the dead layer for both naked samples, MF_1 and MF_2, were found to be 0.6 nm, which is explained by oxidation and different spin orientation at the surface. The silica layer in the coated powders, MFS_1 and MFS_2, was obtained from TEM images to be of the order of 15 nm.

As shown in Table 2, MF_1 NPs have higher coercivity than MF_2, which can be explained by their smaller average size and higher surface/ volume ratio. In the case of coated samples, both show the same coercivity.

3.5. MTT assay

The MTT assay was used to estimate the cytotoxicity of the single-phase Mn ferrite and the SiO_2-coated ones. Fig. 7a, b, and c show the viability of A549 cells at different concentrations (25, 50, 75, 100,125,150 and 175 μg/mL) exposed to 24 h and 48 h measurement. It can be clearly observed that the percent of cell viability depends on the concentration of nanoparticles in the cell culture media and decreases upon increasing nanoparticle concentration [42]. Also, the silica-coated nanoparticles are more biocompatible than the bare particles for the same concentration of samples. This is due to the fact that silica coating protects $MnFe_2O_4$ against acidic erosion which reduces cytotoxicity [64]. At low concentrations, the well-dispersion of nanoparticles occurs, thus, this facilitates their intracellular uptake and inhibits cellular damage [64]. In the opposite limit, at higher concentrations, the overloading of particles yields the fatality of cells. Concentration-dependent cytotoxicity of copper ferrite, potassium ferrite, manganese and zinc ferrite have also been reported [64–66]. The viability of $CuFe_2O_4$ NPs

[65] and $KFeO_2$ [64] at100 g/mL exhibited 81.24% and 87%, respectively, whereas, in the case of silica-coated ones are 125.76% and 91%, respectively, which show the effect of SiO_2 coating. In another literature [66], the viability of $MnFe_2O_4$ at A549 cancer cell with 0.2 mg/mL concentrations obtained 79%, also in the case of $ZnFe_2O_4$, it was 47%. All in all, in this study, for all concentrations of between 24 and 48 h coated or uncoated samples, the values of cell the viability are more than 80%. These results indicate that both prepared samples exhibit low cytotoxicity, satisfying one of the major requirements for biomedical applications. However, the cell viability of $MnFe_2O_4$ and $MnFe_2O_4$ @mSiO₂ NPs witnessed a decrease after 72 h in a dose-dependent manner [67,68]. This stabilized at approximately 40% of that of the control cells in response to NPs concentrations ranging from 150 to 175 μg/mL.

3.6. DAPI

In order to investigate the nuclear alterations of cells by synthesized $MnFe_2O_4$ (MF_1) and silica-coated NPs (MFS_1), they were treated by 691 μg/mL concentration of MF_1 and 566 μg/mL of MFS_1 (these concentrations of powders showed an induction of apoptosis of 50% (IC50) in A549 cells) then after 24 h, cells were stained with DAPI (blue). In comparison with Fig. 7d, Fig. 7e and f, depict all cells that nanoparticles had treated remained healthy due to the low penetration of both nanoparticles into the cells and the high immunity of them which was determined in the MTT test. On the contrary, after 72 h incubation of MFS_1, nanoparticles permeate into the cells and induce cell death (Fig. 7g).
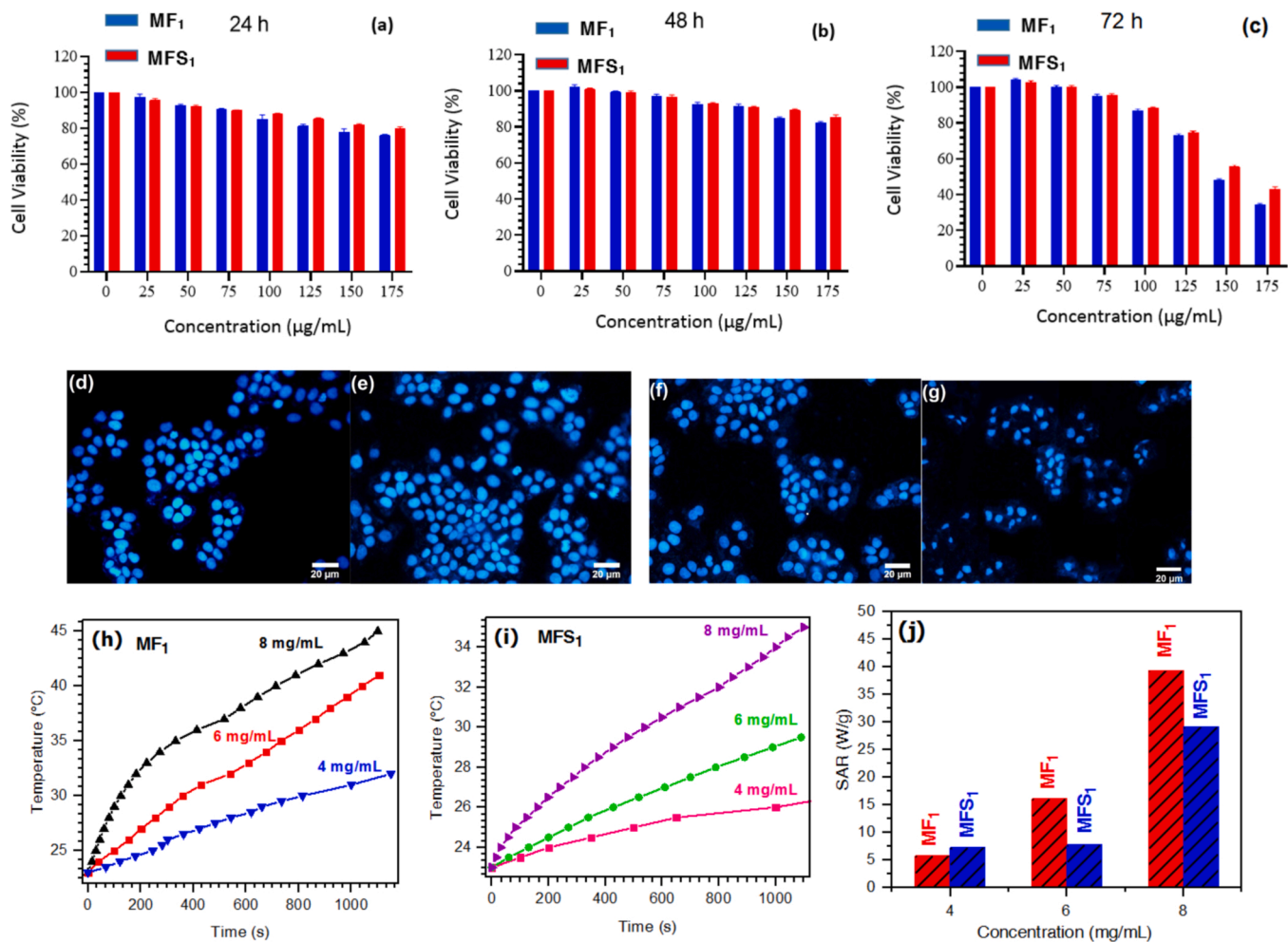
Fig. 7. (a) The cytotoxicity of MnFe$_2$O$_4$ and MnFe$_2$O$_4$ @mSiO$_2$ NPs in A549 cells after 24 h, and (b) 48, and (c) 72 h, (d) control (e) stained cells with DAPI treated for 24 h with MF$_1$ and (f) MFS$_1$ nanoparticles and (g) for 72 h with MFS$_1$ (h) time- temperature dependent curve of MF$_1$ and (i) MFS$_1$ NPs in different concentrations, and (j) SAR as a function of concentration.

3.7. Hyperthermia

The magnetic hyperthermia performance of the single-phase MnFe$_2$O$_4$ and silica-coated NPs at a concentration of 4, 6 and 8 mg/mL in deionized water are shown in Fig. 7h and i. The temperature rise of the aqueous suspensions depends on the concentration of NPs. For the MnFe$_2$O$_4$ NPs (Fig. 7h), the temperature has risen from 23 °C to 45 °C at 128 kHz frequency and 10 kA /m field and 8 mg/mL concentration for 1100 s. While, the temperature of two other samples with concentrations of 6 mg/mL and 4 mg/mL increases to 39 °C and 30 °C, respectively at the same time. This is in good agreement with the results reported for the MnFe$_2$O$_4$ NPs with a 10 mg/mL concentration, at 1.95 MHz and 2300 A/m for 70 s [69].

The mechanism of MNPs heating under an alternating magnetic field, is due to energy losses via magnetic hysteresis and relaxation mechanisms [4,12]. The heat released depends on the frequency, the square of the amplitude of the external field and the type and size of NPs [6,11]. It should be noted that for NPs with negligible coercivity, hysteresis losses are almost absent, and heating arises from N é el and Brownian relaxation mechanisms, the dominant one depending on the particle size and distribution. Typically, for NPs of less than 20 nm is by N é el relaxation dominates while, for larger sizes, Brown relaxation and hysteresis losses are more important [5,12]. This magnetic energy dissipation in ferrofluid samples (Fig. 7j) is measured in terms of specific absorption rate (SAR) that can be obtained from the initial slope of Fig. 7h and i as [4]:

$$SAR_{linear} = \frac{M_{water}}{M_n} \quad C \quad \frac{dT}{dt} \tag{7}$$

where C is the specific heat capacity of suspension equal to 4.186 J/g °C, $\frac{dT}{dt}$ is the initial slope of time-dependent temperature curve, M_{water} and M_n are the specific masses of the water and total ferrite content in the suspension, respectively. According to the size of naked and silica-coated MNPs, the main mechanisms for heat dissipation are expected to be both Brown and N é el relaxation. The SAR values obtained for bare and coated MnFe$_2$O$_4$ samples are 39. W/g and 29. W/g, respectively. The effect of SiO$_2$ coating on SAR value is mainly dependent on the type of basic MNPs [31,57,70]. For example, reported results on silica-coated Fe$_3$O$_4$ [57] and CoFe$_2$O$_4$ and CoFe$_2$O$_4$. SiO$_2$ [70] showed that the coated samples had higher SAR than bare at a magnetic field of 180 Gauss; however, in a lower field (90 Gauss) both of them showed the same SAR. In a different work [71], the silica-coated Fe$_3$O$_4$ NPs exhibited a smaller SAR value than the pristine Fe$_3$O$_4$ NPs. Additionally, according to other work [72] MnFe$_2$O$_4$ NPs showed 120 W/g SLP because of the broad particle size distribution. In this study, results showed that the SAR value of silica-coated samples decreased compared to MnFe$_2$O$_4$ NPs, as well. This is bound to the fact that the silica coating significantly reduces the SAR value by hindering the heat flow, therefore, decreasing the heating efficiency [57]. This means that silica coating on the NPs should be designed to be the minimum necessary to keep the NPs stable in water, as well.
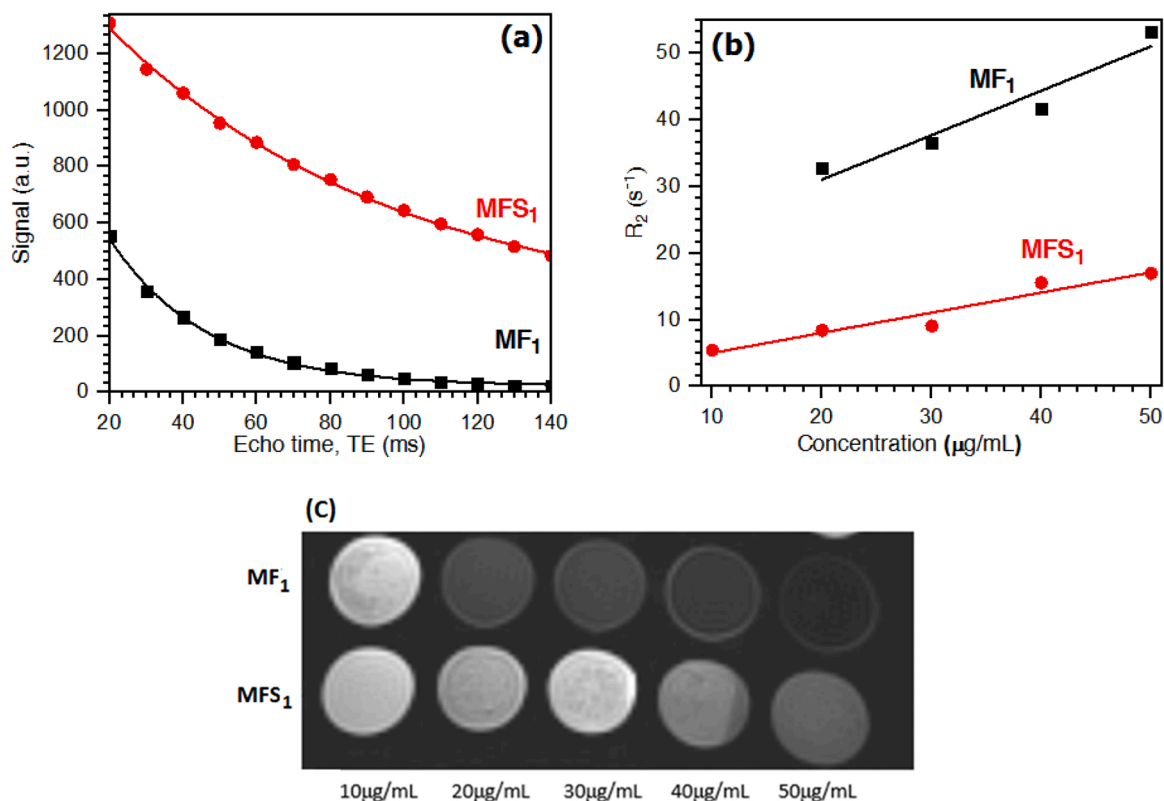
Fig. 8. (a) Signal relaxation curve as a function of TE for different magnetic nanoparticles (MNPs) at concentration of 30 μg/mL (b) Transverse relaxation rate, R_2 versus samples concentration (c) T_2-weighted MRI of nanoparticles with different formulation in 1% agarose phantom at 3.0 T (using multi-echo spin echo (SE) sequence [time to repeat (TR) / time to echo (TE)   3000/30 ms].

3.8. MRI

Fig. 8 show the changes in MRI signal intensity for MF1 and MF1S samples with time and sample concentration. The MF_1 exhibits a higher ability as a T_2 contrast agent with an apparent decrease in MR signals with time and a higher decrease in contrast as concentration increases. The Relaxivity r_2 value of MF_1 was found to be 1.04 μg/mL ^{1}s ^{1} higher than MFS_1 which was 0.32 μg/mL ^{1}s ^{1}. This showed that the ability of MF_1 to induce local magnetic inhomogeneity was higher than MFS_1 and it has the potential to be used as MRI T_2 contrast agent.

For comparison, a study measuring synthesized manganese-ferrite in nanocomposites (14 nm particle size) at 3 T showed a r_2 value of 74 mM ^{1} s ^{1} [73]. Another study of synthesized manganese ferrite nanoparticles coated with silica showed r_2 value of 60.65 mM ^{1} s ^{1} (14 nm particle size) when measured at 4.7 T [74]. When compared with commercial T_2 MRI contrast agents, Ferumoxides (Feridex) developed by AMAG Pharma (hydrodynamic diameter ∼200 nm) reported r_2 value of 98.3 mM ^{1} s ^{1} while Resovist (Ferucarbotran) developed by Schering AG (hydrodynamic diameter > 50 nm) declared r_2 value of 151 mM ^{1} s ^{1} at 1.5 T [75]. Thus, by comparing the r_2 values reported in this study with other manganese-based nanoparticles and commercial T_2 MRI contrast agents, we conclude that MF_1 can be used as an MRI T_2 contrast agent.

4. Conclusion

The $MnFe_2O_4$ NPs were synthesized via a simple, bio-friendly and low-cost hydrothermal route. The NPs were coated with inorganic biocompatible SiO_2 with the assistance of CTAB and TEOS. The effect of different reducing agents NaOH and NH_4OH were explored, indicating the formation of spinel $MnFe_2O_4$ in both cases, single phased in the former case and with small contamination of hematite in the latter one.

In both cases, the manganese ferrite particles were nanosized being smaller in the case of the synthesis with NaOH. For the silica-coated $MnFe_2O_4$ NPs, a bimodal distribution with two average particle sizes of 58 and 150 nm was determined from the TEM images. The samples exhibited the expected ferrimagnetic behaviour. From the MTT assay for all concentrations tested, the values of the cell toxicity were below 20%, $MnFe_2O_4$ @mSiO₂ NPs being more biocompatible than $MnFe_2O_4$ NPs. The high immunity of the cells to these nanoparticles, determined in the MTT test, was explained by DAPI results that confirmed a low penetration of both types of NPs into the cells. The results of MRI indicate that the pristine $MnFe_2O_4$ NPs have the potential to be used as MRI contrast agents with advantages compared to the silica-coated ones. When studied for hyperthermia applications, the $MnFe_2O_4$ @mSiO₂ NPs presented a smaller SAR value than the sample without SiO_2, which can be explained by the increase in the volume of these NPs that increases the associated relaxation time or simply by the mass increase in the normalization process. Summarizing, synthesized $MnFe_2O_4$ are better candidates for MRI and hyperthermia targets than the corresponding silica-coated NPs due to their superior efficiency as a T2 contrast agent while displaying high biocompatibility and low toxicity.

Declaration of Competing Interest

The authors declare that they have no known competing financial interests or personal relationships that could have appeared to influence the work reported in this paper.

References

[1] C. Bárcena, A.K. Sra, G.S. Chaubey, C. Khemtong, J.P. Liu, J. Gao, Zinc ferrite nanoparticles as MRI contrast agents, Chem. Commun. (2008) 2224–2226, https://doi.org/10.1039/b801041b.

[2] J. Lu, S. Ma, J. Sun, C. Xia, C. Liu, Z. Wang, X. Zhao, F. Gao, Q. Gong, B. Song, X. Shuai, H. Ai, Z. Gu, Manganese ferrite nanoparticle micellar nanocomposites as

MRI contrast agent for liver imaging, Biomaterials 30 (2009) 2919–2928, https://doi.org/10.1016/j.biomaterials.2009.02.001.

[3] B.T. Mai, P.B. Balakrishnan, M.J. Barthel, F. Piccardi, D. Niculaes, F. Marinaro, S. Fernandes, A. Curcio, H. Kakwere, G. Autret, R. Cingolani, F. Gazeau, T. Pellegrino, Thermoresponsive iron oxide nanocubes for an effective clinical translation of magnetic hyperthermia and heat-mediated chemotherapy, ACS Appl. Mater. Interfaces 11 (2019) 5727–5739, https://doi.org/10.1021/acsami.8b16226.

[4] A. Hajalilou, L.P. Ferreira, M.E. Melo Jorge, C.P. Reis, M.M. Cruz, Superparamagnetic Ag-Fe3O4 composites nanoparticles for magnetic fluid hyperthermia, J. Magn. Magn. Mater. 537 (2021), 168242, https://doi.org/10.1016/j.jmmm.2021.168242.

[5] A. Rezanezhad, A. Hajalilou, F. Eslami, E. Parvini, Superparamagnetic magnetite nanoparticles for cancer cells treatment via magnetic hyperthermia: effect of natural capping agent, particle size and concentration, J. Mater. Sci. Mater. Electron. 32 (2021) 24026–24040, https://doi.org/10.1007/s10854-021-06865-8.

[6] H. Jalili, B. Aslibeiki, A. Hajalilou, O. Musalu, L.P. Ferreira, M.M. Cruz, Bimagnetic hard/soft and soft/hard ferrite nanocomposites: structural, magnetic and hyperthermia properties, Ceram. Int (2021), https://doi.org/10.1016/J.CERAMINT.2021.11.025.

[7] E. Céspedes, J.M. Byrne, N. Farrow, S. Moise, V.S. Coker, M. Bencsik, J.R. Lloyd, N.D. Telling, Bacterially synthesized ferrite nanoparticles for magnetic hyperthermia applications, Nanoscale 6 (2014) 12958–12970, https://doi.org/10.1039/c4nr03004d.

[8] I. Sharifi, H. Shokrollahi, S. Amiri, Ferrite-based magnetic nanofluids used in hyperthermia applications, J. Magn. Magn. Mater. 324 (2012) 903–915, https://doi.org/10.1016/j.jmmm.2011.10.017.

[9] N.Y. Mostafa, Z.I. Zaki, Z.K. Heiba, Journal of magnetism and magnetic materials structural and magnetic properties of cadmium substituted manganese ferrites prepared by hydrothermal route, J. Magn. Magn. Mater. 329 (2013) 71–76, https://doi.org/10.1016/j.jmmm.2012.09.004.

[10] D. Niculaes, A. Lak, G.C. Anyfantis, S. Marras, O. Laslett, S.K. Avugadda, M. Cassani, D. Serantes, O. Hovorka, R. Chantrell, T. Pellegrino, Asymmetric assembling of iron oxide nanocubes for improving magnetic hyperthermia performance, ACS Nano 11 (2017) 12121–12133, https://doi.org/10.1021/acsnano.7b05182.

[11] V. Pilati, R. Cabreira Gomes, G. Gomide, P. Coppola, F.G. Silva, F.L.O. Paula, R. Perzynski, G.F. Goya, R. Aquino, J. Depeyrot, Core/shell nanoparticles of non-stoichiometric Zn-Mn and Zn-Co ferrites as thermosensitive heat sources for magnetic fluid hyperthermia, J. Phys. Chem. C. 122 (2018) 3028–3038, https://doi.org/10.1021/acs.jpcc.7b11014.

[12] K.K. Kefeni, T.A.M. Msagati, T.T. Nkambule, B.B. Mamba, Spinel ferrite nanoparticles and nanocomposites for biomedical applications and their toxicity, Mater. Sci. Eng. C. 107 (2020), 110314, https://doi.org/10.1016/j.msec.2019.110314.

[13] H. El Moussaoui, T. Mahfoud, S. Habouti, K. El Maalam, M. Ben Ali, M. Hamedoun, O. Mounkachi, R. Masrour, E.K. Hlil, A. Benyoussef, Synthesis and magnetic properties of tin spinel ferrites doped manganese, J. Magn. Magn. Mater. 405 (2016) 181–186, https://doi.org/10.1016/J.JMMM.2015.12.059.

[14] H. El Moussaoui, T. Mahfoud, M. Ben Ali, Z. Mahhouti, R. Masrour, M. Hamedoun, E.K. Hlil, A. Benyoussef, Experimental studies of neodymium ferrites doped with three different transition metals, Mater. Lett. 171 (2016) 142–145, https://doi.org/10.1016/J.MATLET.2016.02.072.

[15] M. Pourzaki, R. Kavkhani, A. Kianvash, A. Hajalilou, Structure, magnetic and transmission characteristics of the Co substituted Mg ferrites synthesized via a standard ceramic route, Ceram. Int. 45 (2019) 5710–5716, https://doi.org/10.1016/j.ceramint.2018.12.036.

[16] A. Hajalilou, S.A. Mazlan, A review on preparation techniques for synthesis of nanocrystalline soft magnetic ferrites and investigation on the effects of microstructure features on magnetic properties, Appl. Phys. A Mater. Sci. Process. 122 (2016), https://doi.org/10.1007/s00339-016-0217-2.

[17] R. Masrour, E.K. Hlil, M. Hamedoun, A. Benyoussef, O. Mounkachi, H. El Moussaoui, Electronic and magnetic structures of Fe3O4 ferrimagnetic investigated by first principle, mean field and series expansions calculations, J. Magn. Magn. Mater. 378 (2015) 37–40, https://doi.org/10.1016/J.JMMM.2014.10.135.

[18] T. Shanmugavel, S.G. Raj, G.R. Kumar, G. Rajarajan, Synthesis and structural analysis of nanocrystalline MnFe2O4, Phys. Procedia 54 (2014) 159–163, https://doi.org/10.1016/j.phpro.2014.10.053.

[19] X.L. Shi, H. Yang, G.Q. Shao, X.L. Duan, Z. Xiong, P. Sun, T.G. Wang, Synthesis of (Mg0.476Mn0.448Zn0.007)(Fe1.997Ti0.002)O4 powder and sintered ferrites by high energy ball-milling process, J. Magn. Magn. Mater. 312 (2007) 347–353, https://doi.org/10.1016/j.jmmm.2006.10.872.

[20] R. Masrour, M. Hamedoun, A. Benyoussef, Magnetic properties of MnCr2O4 nanoparticle, J. Magn. Magn. Mater. 322 (2010) 301–304, https://doi.org/10.1016/J.JMMM.2009.08.051.

[21] K. El Maalam, M. Ben Ali, H. El Moussaoui, O. Mounkachi, M. Hamedoun, R. Masrour, E.K. Hlil, A. Benyoussef, Magnetic properties of tin ferrites nanostructures doped with transition metal, J. Alloy. Compd. 622 (2015) 761–764, https://doi.org/10.1016/J.JALLCOM.2014.10.152.

[22] P. Papazoglou, E. Eleftheriou, V.T. Zaspalis, Low sintering temperature MnZn-ferrites for power applications in the frequency region of 400 kHz, J. Magn. Magn. Mater. 296 (2006) 25–31, https://doi.org/10.1016/j.jmmm.2005.01.021.

[23] E. Erdawati, D. Darsef, Synthesis of magnesium ferrites for the adsorption of congo red from aqueous solution using batch studies, IOP Conf. Ser. Mater. Sci. Eng. 335 (2018), https://doi.org/10.1088/1757-899X/335/1/012024.

[24] M. Ben Ali, K. El Maalam, H. El Moussaoui, O. Mounkachi, M. Hamedoun, R. Masrour, E.K. Hlil, A. Benyoussef, Effect of zinc concentration on the structural and magnetic properties of mixed Co–Zn ferrites nanoparticles synthesized by sol/gel method, J. Magn. Magn. Mater. 398 (2016) 20–25, https://doi.org/10.1016/J.JMMM.2015.08.097.

[25] A. Yusmar, L. Armitasari, E. Suharyadi, Effect of Zn on dielectric properties of Mn-Zn spinel ferrite synthesized by coprecipitation, Mater. Today Proc. 5 (2018) 14955–14959, https://doi.org/10.1016/j.matpr.2018.04.037.

[26] H. El Moussaoui, O. Mounkachi, R. Masrour, M. Hamedoun, E.K. Hlil, A. Benyoussef, Synthesis and super-paramagnetic properties of neodymium ferrites nanorods, J. Alloy. Compd. 581 (2013) 776–781, https://doi.org/10.1016/J.JALLCOM.2013.07.139.

[27] M. Ben Ali, O. Mounkachi, K. El Maalam, H. El Moussaoui, M. Hamedoun, E.K. Hlil, D. Fruchart, R. Masrour, A. Benyoussef, Coexistence of blocked, metamagnetic and canted ferrimagntic phases at high temperature in Co–Nd ferrite nanorods, Superlattices Micro 84 (2015) 165–169, https://doi.org/10.1016/J.SPMI.2015.05.002.

[28] A. Hajalilou, M. Hashim, R. Ebrahimi-Kahrizsangi, M.T. Masoudi, Effect of milling atmosphere on structural and magnetic properties of Ni-Zn ferrite nanocrystalline, Chin. Phys. B. 24 (2015), https://doi.org/10.1088/1674-1056/24/4/048102.

[29] O.M. Hemeda, N.Y. Mostafa, O.H. Abd Elkader, M.A. Ahmed, Solubility limits in Mn-Mg ferrites system under hydrothermal conditions, J. Magn. Magn. Mater. 364 (2014) 39–46, https://doi.org/10.1016/j.jmmm.2014.03.061.

[30] C. Hasirci, O. Karaagac, H. Köçkar, Superparamagnetic zinc ferrite: a correlation between high magnetizations and nanoparticle sizes as a function of reaction time via hydrothermal process, J. Magn. Magn. Mater. 474 (2019) 282–286, https://doi.org/10.1016/j.jmmm.2019.01.025.

[31] Y. Iqbal, H. Bae, I. Rhee, S. Hong, Magnetic heating of silica-coated manganese ferrite nanoparticles, J. Magn. Magn. Mater. 409 (2016) 80–86, https://doi.org/10.1016/j.jmmm.2016.02.078.

[32] Z. Rashid, M. Soleimani, R. Ghahremanzadeh, M. Vossoughi, E. Esmaeili, Effective surface modification of MnFe 2 O 4 @SiO 2 @PMIDA magnetic nanoparticles for rapid and high-density antibody immobilization, Appl. Surf. Sci. 426 (2017) 1023–1029, https://doi.org/10.1016/j.apsusc.2017.07.246.

[33] C. Cannas, A. Musinu, A. Ardu, F. Orrù, D. Peddis, M. Casu, R. Sanna, F. Angius, G. Diaz, G. Piccaluga, CoFe2O4 and cofe2o4/sio 2 core/shell nanoparticles: magnetic and spectroscopic study, Chem. Mater. 22 (2010) 3353–3361, https://doi.org/10.1021/cm903837g.

[34] R. Kavkhani, M. Pourzaki, A. Kianvash, A. Hajalilou, R.G. Adli, Effect of sintering temperature and soaking time on the magnetic properties and transmission behavior of nano crystalline Mg0.8Mn0.2Al0.1Fe1.9O4, J. Sol. -Gel Sci. Technol. 99 (2021) 444–454, https://doi.org/10.1007/S10971-020-05454-1.

[35] Z. Gao, X. Liu, G. Deng, F. Zhou, L. Zhang, Q. Wang, J. Lu, Fe3O4@mSiO2-FA-CuS-PEG nanocomposites for magnetic resonance imaging and targeted chemo-photothermal synergistic therapy of cancer cells, Dalt. Trans. 45 (2016) 13456–13465, https://doi.org/10.1039/c6dt01714b.

[36] T. Zhao, N.T. Nguyen, Y. Xie, X. Sun, Q. Li, X. Li, Inorganic nanocrystals functionalized mesoporous silica nanoparticles: fabrication and enhanced bio-applications, Front. Chem. 5 (2017) 1–8, https://doi.org/10.3389/fchem.2017.00118.

[37] B.G. Cha, J. Kim, Functional mesoporous silica nanoparticles for bio-imaging applications, Wiley Interdiscip. Rev. Nanomed. Nanobiotechnol. 11 (2019) 1–22, https://doi.org/10.1002/wnan.1515.

[38] Z. Sharafi, B. Bakhshi, J. Javidi, S. Adrangi, Synthesis of silica-coated iron oxide nanoparticles: preventing aggregation without using additives or seed pretreatment, Iran J. Pharm. Res 17 (2018) 386–395, https://doi.org/10.22037/ijpr.2018.2160.

[39] A. Bali Ogholbeyg, A. Kianvash, A. Hajalilou, E. Abouzari-Lotf, A. Zarebkohan, Cytotoxicity characteristics of green assisted-synthesized superparamagnetic maghemite (γ-Fe2O3) nanoparticles, J. Mater. Sci. Mater. Electron. 29 (2018) 12135–12143, https://doi.org/10.1007/s10854-018-9321-8.

[40] A. Hajalilou, M. Hashim, M. Nahavandi, I. Ismail, Mechanochemical carboaluminothermic reduction of rutile to produce TiC-Al2O3 nanocomposite, Adv. Powder Technol. 25 (2014) 423–429, https://doi.org/10.1016/j.apt.2013.07.004.

[41] A. Hajalilou, S.A. Mazlan, K. Shameli, A comparative study of different concentrations of pure Zn powder effects on synthesis, structure, magnetic and microwave-absorbing properties in mechanically-alloyed Ni-Zn ferrite, J. Phys. Chem. Solids (96–97) (2016) 49–59, https://doi.org/10.1016/j.jpcs.2016.05.001.

[42] S. Kanagesan, S.B.A. Aziz, M. Hashim, I. Ismail, S. Tamilselvan, N.B.B.M. Alitheen, M.K. Swamy, B.P.C. Rao, Synthesis, characterization and in vitro evaluation of manganese ferrite (MnFe2O4) nanoparticles for their biocompatibility with murine breast cancer cells (4T1), Molecules 21 (2016) 1–9, https://doi.org/10.3390/molecules21030312.

[43] A. Hajalilou, M. Hashim, M. Taghi Masoudi, A comparative study of in-situ mechanochemically synthesized Mn0.5Zn0.5Fe2O4 ferrite nanoparticles in the MnO/ZnO/Fe2O3 and MnO2/Zn/Fe2O3 systems, Ceram. Int. 41 (2015) 8070–8079, https://doi.org/10.1016/j.ceramint.2015.03.005.

[44] R.A. Varin, A.S. Bidabadi, M. Polanski, M. Biglari, L. Stobinski, The effects of filamentary Ni, graphene and lithium amide (LiNH2) additives on the dehydrogenation behavior of mechano-chemically synthesized crystalline manganese borohydride (Mn(BH4)2) and its solvent filtration/extraction, Mater. Res. Bull. 100 (2018) 394–406, https://doi.org/10.1016/j.materresbull.2017.12.051.

[45] R. Zandipak, S. Sobhan Ardakani, A. Shirzadi, Synthesis and application of nanocomposite Fe3O4@SiO2@CTAB–SiO2 as a novel adsorbent for removal of

cyclophosphamide from water samples, Sep. Sci. Technol. 55 (2020) 456–470, https://doi.org/10.1080/01496395.2019.1566262.

[46] N. Li, F. Fu, J. Lu, Z. Ding, B. Tang, J. Pang, Facile preparation of magnetic mesoporous MnFe2O4@SiO2 CTAB composites for Cr(VI) adsorption and reduction, Environ. Pollut. 220 (2017) 1376–1385, https://doi.org/10.1016/j.envpol.2016.10.097.

[47] B. Sahoo, K.S.P. Devi, S. Dutta, T.K. Maiti, P. Pramanik, D. Dhara, Biocompatible mesoporous silica-coated superparamagnetic manganese ferrite nanoparticles for targeted drug delivery and MR imaging applications, J. Colloid Interface Sci. 431 (2014) 31–41, https://doi.org/10.1016/j.jcis.2014.06.003.

[48] R.L. Dhiman, S.P. Taneja, V.R. Reddy, Preparation and characterization of manganese ferrite aluminates, Adv. Condens. Matter Phys. 2008 (2008) 1–7, https://doi.org/10.1155/2008/703479.

[49] K.B. Modi, N.H. Vasoya, V.K. Lakhani, T.K. Pathak, Magnetic phase evolution and particle size estimation study on nanocrystalline Mg–Mn ferrites, Appl. Nanosci. 5 (2015) 11–17, https://doi.org/10.1007/s13204-013-0287-9.

[50] A. Baykal, S. Güner, A. Demir, S. Esir, F. Genç, Effect of zinc substitution on magneto-optical properties of Mn 1-xZnxFe2O4/SiO2 nanocomposites, Ceram. Int. 40 (2014) 13401–13408, https://doi.org/10.1016/j.ceramint.2014.05.059.

[51] H.M. Xiao, X.M. Liu, S.Y. Fu, Synthesis, magnetic and microwave absorbing properties of core-shell structured MnFe2O4/TiO2 nanocomposites, Compos. Sci. Technol. 66 (2006) 2003–2008, https://doi.org/10.1016/j.compscitech.2006.01.001.

[52] F. Zeb, K. Nadeem, S.K.A. Shah, M. Kamran, I.H. Gul, L. Ali, Surface spins disorder in uncoated and SiO2 coated maghemite nanoparticles, J. Magn. Magn. Mater. 429 (2017) 270–275, https://doi.org/10.1016/j.jmmm.2017.01.040.

[53] U. Kurtan, M. Amir, A. Yildiz, A. Baykal, Synthesis of magnetically recyclable MnFe 2 O 4 @SiO 2 @Ag nanocatalyst: its high catalytic performances for azo dyes and nitro compounds reduction, Appl. Surf. Sci. 376 (2016) 16–25, https://doi.org/10.1016/j.apsusc.2016.02.120.

[54] J.L. Ortiz-Quiñonez, U. Pal, Borohydride-assisted surface activation of Co3O4/CoFe2O4 composite and its catalytic activity for 4-nitrophenol reduction, ACS Omega 4 (2019) 10129–10139, https://doi.org/10.1021/acsomega.9b00118.

[55] V. Jeseentharani, M. George, B. Jeyaraj, A. Dayalan, K.S. Nagaraja, Synthesis of metal ferrite (MFe2O4, M = Co, Cu, Mg, Ni, Zn) nanoparticles as humidity sensor materials, J. Exp. Nanosci. 8 (2013) 358–370, https://doi.org/10.1080/17458080.2012.690893.

[56] F.J. Sotomayor, K.A. Cychosz, M. Thommes, Characterization of micro/mesoporous materials by physisorption: concepts and case studies, ACC Mater. Surf. Res. 3 (2018) 34–50.

[57] S. Larumbe, C. Gómez-Polo, J.I. Pérez-Landazábal, J.M. Pastor, Effect of a SiO2 coating on the magnetic properties of Fe3O4 nanoparticles, J. Phys. Condens. Matter 24 (2012) 266007, https://doi.org/10.1088/0953-8984/24/26/266007.

[58] Y. Ahn, E.J. Choi, S. Kim, H.N. Ok, Magnetization and Mössbauer study of cobalt ferrite particles from nanophase cobalt iron carbonate, Mater. Lett. 50 (2001) 47–52, https://doi.org/10.1016/S0167-577X(00)00412-2.

[59] B. Aslibeiki, M.H. Ehsani, F. Nasirzadeh, M.A. Mohammadi, The effect of interparticle interactions on spin glass and hyperthermia properties of Fe3O4 nanoparticles, Mater. Res. Express 4 (2017), https://doi.org/10.1088/2053-1591/aa7eb1.

[60] B. Aslibeiki, P. Kameli, H. Salamati, G. Concas, M.S. Fernandez, A. Talone, G. Muscas, D. Peddis, Co-doped MnFe2O4 nanoparticles: magnetic anisotropy and interparticle interactions, Beilstein J. Nanotechnol. 10 (2019) 856–865, https://doi.org/10.3762/BJNANO.10.86.

[61] K.L. Livesey, S. Ruta, N.R. Anderson, D. Baldomir, R.W. Chantrell, D. Serantes, Beyond the blocking model to fit nanoparticle ZFC/FC magnetisation curves, Sci. Rep. 8 (2018) 1–9, https://doi.org/10.1038/s41598-018-29501-8.

[62] L. Kafrouni, O. Savadogo, Recent progress on magnetic nanoparticles for magnetic hyperthermia, Prog. Biomater. 5 (2016) 147–160, https://doi.org/10.1007/s40204-016-0054-6.

[63] A.G. Kolhatkar, A.C. Jamison, D. Litvinov, R.C. Willson, Tuning Magn. Prop. Nanopart. (2013), https://doi.org/10.3390/ijms140815977.

[64] L. Khanna, N.K. Verma, Silica/potassium ferrite nanocomposite: Structural, morphological, magnetic, thermal and in vitro cytotoxicity analysis, Mater. Sci. Eng. B Solid-State Mater. Adv. Technol. 178 (2013) 1230–1239, https://doi.org/10.1016/j.mseb.2013.08.004.

[65] L. Khanna, G. Gupta, S.K. Tripathi, Effect of size and silica coating on structural, magnetic as well as cytotoxicity properties of copper ferrite nanoparticles, Mater. Sci. Eng. C 97 (2019) 552–566, https://doi.org/10.1016/j.msec.2018.12.051.

[66] C. Iacovita, A. Florea, L. Scorus, E. Pall, R. Dudric, A.I. Moldovan, R. Stiufiuc, R. Tetean, C.M. Lucaciu, Hyperthermia, cytotoxicity, and cellular uptake properties of manganese and zinc ferrite magnetic nanoparticles synthesized by a polyol-mediated process, Nanomaterials 9 (2019) 1–23, https://doi.org/10.3390/nano9101489.

[67] S.A. Thomas, D. Nandan, J. Kass, N.E. Reiner, Countervailing, time-dependent effects on host autophagy promotes intracellular survival of Leishmania, J. Biol. Chem. 293 (2018) 2617–2630, https://doi.org/10.1074/jbc.M117.808675.

[68] S.W. Shin, K. Yang, M. Lee, J. Moon, A. Son, Y. Kim, S. Choi, D.H. Kim, C. Choi, N. Lee, H.C. Park, Manganese ferrite nanoparticles enhance the sensitivity of hepa1–6 hepatocellular carcinoma to radiation by remodeling tumor microenvironments, Int. J. Mol. Sci. 22 (2021) 1–15, https://doi.org/10.3390/ijms22052637.

[69] A. Doaga, A.M. Cojocariu, W. Amin, F. Heib, P. Bender, R. Hempelmann, O. F. Caltun, Synthesis and characterizations of manganese ferrites for hyperthermia applications, Mater. Chem. Phys. 143 (2013) 305–310, https://doi.org/10.1016/j.matchemphys.2013.08.066.

[70] M.E. Cano, R.H. Medina, V.V.A. Fernández, P.E. García-Casillas, Magnetic heating ability of silica-cobalt ferrite nanoparticles, Rev. Mex. Ing. Quim. 13 (2014) 555–561.

[71] C. Tao, Y. Zhu, Magnetic mesoporous silica nanoparticles for potential delivery of chemotherapeutic drugs and hyperthermia, Dalt. Trans. 43 (2014) 15482–15490, https://doi.org/10.1039/c4dt01984a.

[72] M.M. Cruz, L.P. Ferreira, J. Ramos, S.G. Mendo, A.F. Alves, M. Godinho, M. D. Carvalho, Enhanced magnetic hyperthermia of CoFe2O4and MnFe2O4nanoparticles, J. Alloy. Compd. 703 (2017) 370–380, https://doi.org/10.1016/j.jallcom.2017.01.297.

[73] B. Sana, C.L. Poh, S. Lim, A manganese–ferritin nanocomposite as an ultrasensitive T2 contrast agent, Chem. Commun. 48 (2012) 862–864, https://doi.org/10.1039/c1cc15189d.

[74] A. Ahmad, H. Bae, I. Rhee, Highly stable silica-coated manganese ferrite nanoparticles as high-efficacy T2 contrast agents for magnetic resonance imaging, AIP Adv. 8 (2018), https://doi.org/10.1063/1.5027898.

[75] J. Estelrich, M.J. Sánchez-Martín, M.A. Busquets, Nanoparticles in magnetic resonance imaging: From simple to dual contrast agents, Int. J. Nanomed. 10 (2015) 1727–1741, https://doi.org/10.2147/IJN.S76501.